C: Surfaces, Interfaces, Porous Materials, and Catalysis

Highly Efficient Ni-Doped Iron Catalyst for Ammonia Synthesis from QM-Based Hierarchical High Throughput Catalyst Screening

Molly Mcdonald, Jon Fuller, Alessandro Fortunelli, William A. Goddard, and Qi An

J. Phys. Chem. C, **Just Accepted Manuscript** • DOI: 10.1021/acs.jpcc.9b04386 • Publication Date (Web): 20 Jun 2019

Highly Efficient Ni-Doped Iron Catalyst for Ammonia Synthesis from QM-Based Hierarchical High Throughput Catalyst Screening

Molly Mcdonald[1], Jon Fuller[1], Alessandro Fortunelli[2,3*], William A. Goddard[2*], and Qi An[1*]

[1]Department of Chemical and Materials Engineering, University of Nevada – Reno, Nevada 89577, United States
[2]Materials and Procs Simulation Center (MSC), California Institute of Technology, Pasadena, California 91125, United States
[3]CNR-ICCOM, Consiglio Nazionale delle Ricerche, ThC2-Lab, Pisa, 56124, Italy
*Corresponding authors email: alessandro.fortunelli@cnr.it, wag@wag.caltech.edu, qia@unr.edu

Abstract

To discover more efficient industrial catalysts for ammonia synthesis via the Haber-Bosch (HB) process, we employed quantum-mechanics (QM)-based hierarchical high throughput catalyst screening (HHTCS) to test a wide group of elements (34) as candidates to dope the Fe(111) catalyst subsurface. The QM free-energy reaction network of HB over Fe(111) yields ten barriers as potentially rate-determining, of which we select four as prototypical, arrange them hierarchically, and define a corresponding set of screening criteria, which we then use to screen candidate catalysts. This leads to two promising candidates (Co and Ni), from which we selected the most promising (Ni) for a complete QM and kinetic study. The kinetic Monte Carlo (kMC) simulations predict a 16-fold increase in HB turn over frequency (TOF) for the Ni-doped catalyst compared to the pure Fe(111) surface under realistic conditions. The 16-fold increase in HB turn over frequency (TOF) is a significant improvement and may trigger future experimental studies to validate our prediction. This TOF improvement could lead to similar reaction rates as with pure Fe but at areaction temperature decreased by 100 degrees from 773 to 673 K and a total reactant pressure decreased by 6 times from 201 atm to 34 atm. We interpret the reasons underlying this improvement using Valence Bond and kinetic analyses. We suggest this Ni-doped Fe(111) catalyst as a candidate to reduce the world energy consumption for the HB process while satisfying future needs for energy and environment.

1. Introduction

The Haber-Bosch (HB) synthesis of ammonia (NH_3) from atmospheric nitrogen gas (N_2) and hydrogen gas (H_2) extracted from natural gas remains one of the most important industrial chemistry processes. About 150 million tons of NH_3 are produced annually, and then converted into nitrate-based fertilizers needed in agriculture. This process uses 2% of the world's energy and generates more than 300 million tons of carbon dioxide annually due to extremely high operating pressures (50-200 atm) and temperatures (700-850 K).[1-6] Thus, it is essential to develop more efficient catalysts and methods to lower energy consumption and reduce emission of greenhouse gases for both energy and environment requirements.

The catalyst used in industrial settings is iron-based,[1] achieving up to 70% efficiency[6] for the HB process. Other catalysts have been studied, such as ruthenium-based,[7] that can have higher activity at lower pressures and temperatures compared to the iron catalysts, and can be optimized via support engineering, or including promoters,[8,9] but Ru forms toxic compounds[10] and as a precious metal is scarce and therefore expensive to use.[9]

Alternative research lines have explored a (photo-)electrochemical route.[11] Zhou *et al.*[12] showed that N_2 solubility in ionic liquids can allow the electro-reduction of N_2 to ammonia at room temperatures and atmospheric pressures, reaching an efficiency of up to 60%, but concluded that further development is needed on the catalysts used in the ionic solutions. Ogura *et al.*[13] researched the photo-assisted electrochemical reduction of NO to NH_3 with a p-type gallium arsenide electrode in the presence of a transition metal as a catalyst, reaching an efficiency of 22-32% at room temperature and atmospheric pressure, but a large amount of the NO does not convert, due to the inability of the catalyst to complex with NO.[13] Furuya *et al.*[14] used an electrode containing inorganic compounds such as metals and metal oxides at room temperature and pressure, but the efficiency was low. In short, (photo-)electrochemical approaches show promise in reducing energy consumption of the HB process, but Fe-based catalysts are predominately used in industry because of their higher efficiency and low cost.

We initiated a project to use QM computational methods to determine the catalytic mechanism underlying the HB process on Fe-bcc(111)-based catalysts, and we are now using this mechanism to optimize the process. We previously reported the first detailed reaction pathway for the Haber-Bosch process on Fe(111) surface (based on a (2 × 2) surface model).[15] We carried out QM based free energy calculations on all 24 reaction intermediates important at 400 °C and 20 atm, and we determined the reaction free energy barriers for all 12 important reaction steps. Then we included all 24 species and 12 reaction steps in a 45 minute kinetic Monte Carlo analysis. We predicted a turn over frequency (TOF) on the pure Fe(111) surface of 17.7 NH_3/s, in excellent agreement with the single-crystal-experimental results of 9.7 NH_3/s under these conditions.[15] This indicates that our effective activation barrier is only 0.04 eV lower than experiment.

This complete analysis entails significant computational resources, making it impractical for scanning a large number of possibilities. Thus to discover novel catalyst modifications that would increase the rates, we developed an alternative method: **hierarchical high throughput catalyst screening (HHTCS)**, which we applied earlier to select the most promising elements to dope the top layer of the Fe(111) surface.[16] The HHTCS method enables a quick assessment of the effect of dopants on the reaction pathway by predicting how the dopant affects the potentially rate-determining reaction barriers.[16] This allowed us to select out of 34 candidates that Rh and Pt are the most promising top-layer dopants for Fe(111) surface with a predicted increase in TOF of ~3.3 compared to the pure Fe(111) surface. The details of HHTCS approach are published .[16]

To design even more efficient Fe-based catalyst, we now apply the HHTCS approach to finding the best subsurface doping for the Fe (111) surface. We considered the same set of 34 element as single dopants

in a (2 × 2) unit cell of Fe bcc(111), corresponding to 25% subsurface doping as illustrated in Fig. 1. We chose stability in the second layer as first selection criterion, i.e., we require that the dopant prefers second layer over first layer or third layer doping. We consider that stability of the second layer vs the third layer doping may prevent the dopants from going into the bulk, allowing a much lower overall doping so that expensive dopants might be practical. From the initial group of 34 elements, all but three were discarded based on this stability criterion. The surviving three: Ni, Co, and Cr, were then tested against further criteria. All were predicted to decrease the HB overall reaction barrier, but Cr was discarded on the basis of our H_2 poisoning criterion. Ni showed the greatest promise in reducing the overall barrier. Thus for the Ni-doped Fe(111) surface we constructed a full QM-based free-energy diagram and conducted kinetic Monte Carlo (kMC) simulations to predict HB production rate of NH_3. **The predicted TOF** with 0.25 ML doping of Ni in the 2nd layer of Fe(111) at 673 K, and $P(H_2)$ = 15 atm, $P(N_2)$ = 5 atm, $P(NH_3)$ = 1 atm **is 72 NH_3/s** per (2 × 2) site compared to 4.45 NH_3/s on the pure Fe(111) surface for the same conditions. This corresponds to **a 16-fold improvement** which would translate ito a signicant improvement in the HB process. Future HB experiments may focus on Ni doped Fe catalysis to validate our theoretical prediction.

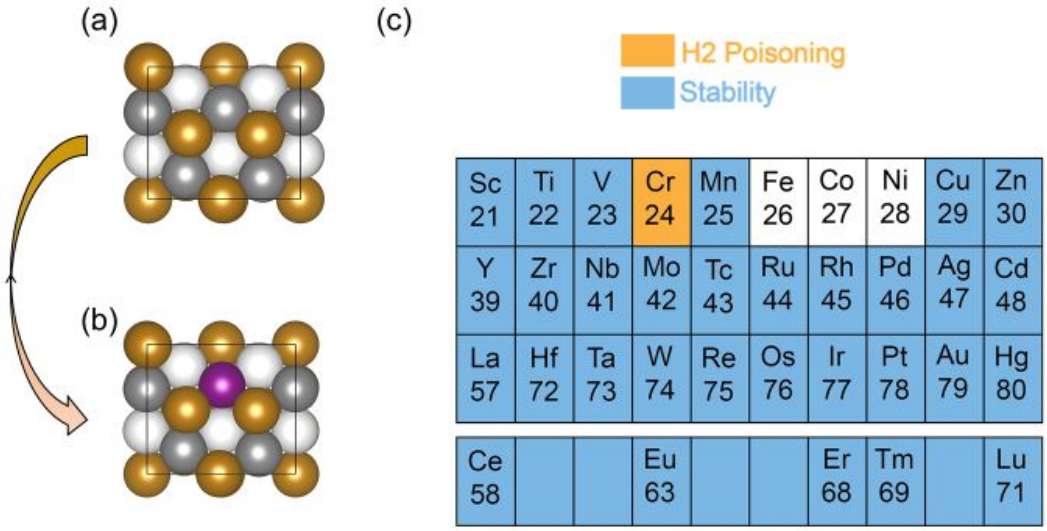

Figure 1. The location of the doping element in the second layer of the Fe(111) surface is shown in purple on the left. (a) shows the pure Fe(111) surface, (b) shows the doped surface: top layer Fe atoms in orange, second layer Fe atoms in gray (Fe) or purple (dopant), third layer Fe atoms in white. (c) depicts the candidate dopant elements (34 elements) and which criterion they failed to pass highlighted in color.

2. QM Computational Details

The free-energy reaction network for NH_3 synthesis over Fe(111) determined in our previous studies[15] was used as the starting point. This is based on density-functional theory (DFT)[17-20] to calculate the electronic energy of the Fe(111) surface in various configurations on a (2 × 2) unit cell using the Perdew-Burke-Ernzerhof exchange-correlation functional with the D3 empirical van der Waals corrections (PBE-D3).[17,18] All calculations were performed using the VASP[21-24] software package, with the projector augmented wave method (PAW) to generate the pseudopotential. In all calculations we used an energy convergence threshold of 10^{-6} eV and a force criterion of 10^{-3} eV/Å. The K-point sampling was chosen to be 4 × 4 × 1 in which z direction is the vacuum direction. All calculations were spin-polarized.

Free-energy corrections were included to obtain the free energy diagram for the HB reaction.[15,16] The zero-point energy, entropy, and enthalpy at 673 °K were derived from the phonon vibrations using harmonic approximation. Then the free energy of various adsorbates states can be derived from G = H TS where H is the enthalpy, S is the entropy and T is the temperature at reaction conditions (673 K). To obtain the full reaction energy diagram, we selected a reference state $3N\_NH_2$ and set its free energy to zero. Then all the free energy of other states were derived by the free energy difference between the state and the reference state plus the possible gas phase species. To correct the free energy of gas species for pressure, we assume an ideal gas and add RT × ln(P2/P1) with a reference pressure of P = 1 atm. The transition states between various absorbances were obtained using the climbing image NEB approach (CINEB). Eight intermediate images were optimized in CINEB approach, excluding initial and final images. The simulation details can be found in previous work.[15,16]

3. Hierarchical High-Throughput Catalyst Screening (HHTCS) Approach

The hierarchical high-throughput catalyst screening (HHTCS) approach[16] was used to determine the most promising candidates for reducing the free-energy barriers of the rate-determining steps at 673 °K and 20 atm. HHTCS needs as a starting point the reaction network for a catalyst, in this case HB on the Fe bcc(111) surface,[15] shown in Fig. 2a at 673 K and pressures of H_2 = 15 atm, N_2 = 5 atm, and NH_3 = 1 atm, which we consider realistic target conditions for a less-energy intensive HB process. The four prototypical (or primary) barriers chosen as potentially rate-determining are indicated with colored arrows for clarity in Fig. 2a and Fig. 2b-b.

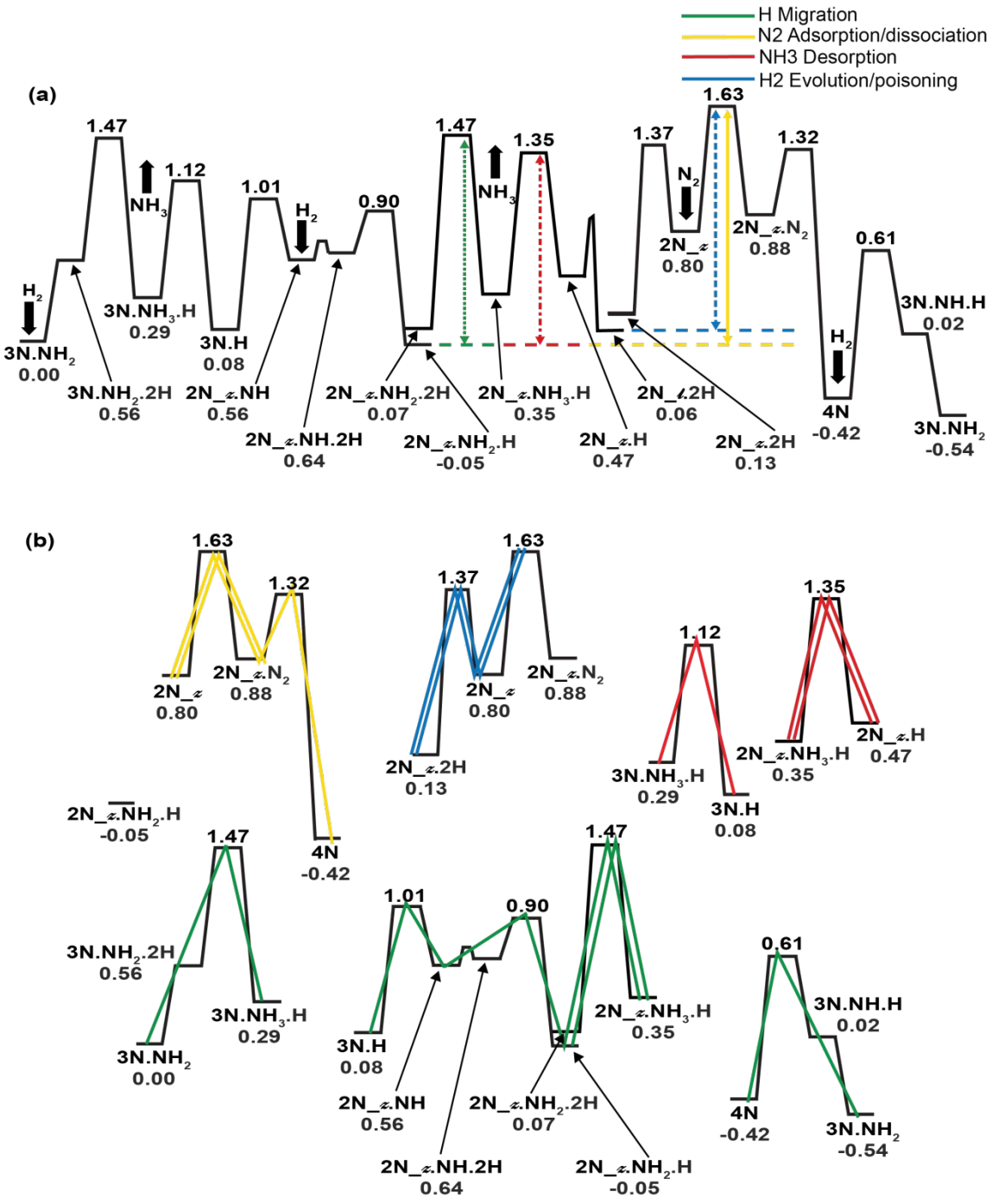

Figure 2. (a) Standard free-energy diagram (minimum barrier path) of the Haber-Bosch process on the Fe(111) surface at 673 K, $P(H_2)$ = 15 atm, $P(N_2)$ = 5 atm, $P(NH_3)$ = 1 atm (free energies in eV). The four prototypical free-energy barriers used to define screening criteria are indicated with arrows in different colors: adsorption/dissociation of N_2 in yellow, H migration in green, H_2 poisoning in blue, and NH_3 desorption in red. Reprinted (adapted) with permission from reference 16. Copyright (2018) American Chemical Society. (b) Same diagram as (a), with the 4 groups of reaction steps separated into separate images to have a clearer picture of the energy barriers of each group. The highest energy barrier, which we take as prototypical for the given group, is indicated with a double line. N_2 adsorption in yellow, H_2 poisoning blue, and NH_3 desorption in red, H migration in green.

Fig. 2b explains the reasons of our choice and illustrates the philosophy behind the HHTCS approach. The shortest (minimum barrier, or Dijkstra[25] path between initial and final states within the HB reaction network on Fe(111) is characterized by 10 different potentially rate-determining steps. We group these 10 steps into 4 sets by chemical analogy and distinguish them by different colors in Fig. 2b:

- adsorption/dissociation of N_2 in yellow,
- H migration (i.e., H addition to NH_x to form an NH_{x+1}) in green,
- H_2 poisoning (i.e., H_2 adsorption/evolution) in blue, and
- NH_3 desorption in red.

We then take the steps of each group having the highest-energy transition state as prototypical (the 4 prototypical steps are indicated by double lines in Fig. 2b), assuming that the energetics of the other steps in a given group as a function of catalyst composition will follow the same trend as the prototypical one. To test this assumption, for the doped system with the best expected catalytic efficiency (in this case, subsurface Ni) we computed the full energy diagram.

We next single out the states that are potentially "dynamical resting states" in the HB free-energy profile, i.e., the states leading to a deep minimum in the steady-state free-energy diagram, which for Fe(111) under the given conditions are: 2N_ȝ.NH_2.H and 2N_ȓ.2H where ȝ and ȓ represent zig-zag and linear N configurations, respectively.

The next stage of the HHTCS protocol is illustrated in Fig. S1 and Fig. S2 of Supporting Information (SI), which leads us back to Fig. 2a: the barrier of each prototypical step is defined to start from the preceding closest dynamical resting state, to finally define the 4 prototypical barriers needed for screening.

The final stage of the HHTCS protocol is to arrange hierarchically the prototypical barriers in decreasing value, to define for each one of them a simple criterion to screen candidate catalysts, and then to implement these criteria to screen the candidate dopants in hierarchical sequence.

In the present work, we considered a set of 34 elements to replace one of the *second* layer Fe atoms in the (2 × 2) unit cell, as depicted in Fig. 1. The HHTCS protocol in the present case of subsurface dopants then reads as follows:

a. Test the stability of dopants in 2nd layer vs. top or third layer, select only the ones preferring 2nd layers for subsequent steps
b. Determine the prototypical (or primary) barriers from the free energy diagram as discussed above and arrange them in a decreasing order
c. Define criteria to estimate the effect of each candidate on the barriers
d. Evaluate each criterion and restrict each screening stage to the elements that have passed previous screening and show a potential in decreasing the overall barrier

e. For the most promising element that passed all screening criteria, reconstruct the full free-energy diagram and use its data as input for kMC simulations to predict actual catalytic efficiency.

Further details can be found in our previous article.[16]

3.1 Screening Criteria

The four primary rate-determining barriers for HB over Fe(111), as discussed above,[16] involve: adsorption/dissociation of N_2, H addition to NH_x to form an NH_{x+1}, H_2 poisoning, and NH_3 desorption, plus a stability criterion. In the following, ΔE is the electronic (QM) energy difference, and the constants appearing in the equations (i.e., 0.102 eV, etc.) are based on free-energy corrections of the pure Fe(111) surface.

Criterion 1: Since we focus on subsurface doping, we put a stability test as a first screening criterion instead of the last criterion as in our previous HHTCS approach,[16] and test the stability of dopants in the second layer with respect to the top (or 3rd) layer. The 4N configuration is used for the stability test, as follows:

$$\text{Barrier (1)} = \Delta E\{4N[\text{subsurface} - \text{dopant}] \rightarrow 4N\,[\text{surface (or 3rd layer)} - \text{dopant}]\} < 0 \qquad (1)$$

where 4N[subsurface – dopant] and 4N[surface (or 3rd layer) – dopant] correspond to configurations with the dopant in the subsurface and surface (or 3rd) layers, respectively. We note in general that the elements discarded by this stability test could be reconsidered in a second stage via a more refined analysis. First, if doping in other sites is energetically preferred, its effect on HB rate should nevertheless be tested. Second, an element segregating e.g. in the third layer could be still effective as a second-layer dopant if it generates a small total HB barrier, where we define the total HB barrier as the sum of the overall HB barrier plus the energy cost of moving the dopant from the third to the second layer. Third, a doping level higher than 0.25 ML could finally be considered so as to produce a partial occupation of the second layer site.

Criterion 2: The largest prototypical barrier in the diagram of Fig. 2a corresponds to the free-energy difference between the $2N\__3.NH_2.H$ dynamical resting state and the saddle point for nitrogen (N_2) adsorption over the $2N\__3$ state ($2N\__3 \rightarrow 2N\__3.N2$). An improved catalyst should decrease this energy and therefore the strength with which the N atoms bind to the surface, while still allowing the nitrogen to dissociate effectively. We translate this into the following criterion:

$$\text{Barrier (2)} = \Delta E\{2N\__3.NH_2.H \rightarrow 2N\__3 + NH_3\} - 0.102 \text{ eV} \qquad (2)$$

$$\text{Constraint: } \Delta E\{2N\__3.N_2[\gamma] \rightarrow 2N\__3 + N_2\} > 0.5 \text{ eV} \qquad (3)$$

where $2N\__3.NH_2.H$, $2N\__3$, and $2N\__3.N_2[\gamma]$ are surface configurations on Fe(111), and N_2 and NH_3 are molecules in the gas phase. It should be emphasized that this prototypical barrier can be decomposed into the sum of 2 terms: (a) the free-energy paid by the system to go from the $2N\__3.NH_2.H$ dynamical resting state to the $2N\__3$ intermediate state; and (b) the N_2 adsorption barrier, i.e., the free-energy barrier from the $2N\__3$ intermediate state to the saddle point for nitrogen (N_2) adsorption over this $2N\__3$ state. As we will see below, this analysis will help us understand why subsurface Ni doping is beneficial for increasing the HB rate.

Criterion 3: The second barrier on the diagram of Fig. 2a is hydrogen poisoning, associated with the process: $2N\__3 \rightarrow 2N\__f.2H$. This corresponds to the possibility that $2N\__f.2H$ becomes the dynamical resting state, and is translated into the formula:

$$\text{Barrier (3)} = \Delta E\{2N\__f.2H \rightarrow 2N\__3 + H_2\} + 0.113 \text{ eV} \qquad (4)$$

Criterion 4: The third barrier is related to hydrogenation of an NH_x to a NH_{x+1} species. The prototypical hydrogenation barrier is: $2N\__3.NH_2.2H \rightarrow 2N\__3.NH_3.H$. We invoke the Brønsted-Evans-Polanyi principle to estimate the energy barrier of this step as a linear function of the energy difference between the configurations: $2N\__3.NH_2.H$ and $2N\__3.NH_3.H$, thus giving the formula:

$$\text{Barrier (4)} = \Delta E\{2N\__3NH_2.H + \tfrac{1}{2}H_2 \rightarrow 2N\__3.NH_3.H\} + 1.549 \text{ eV} \quad (5)$$

Criterion 5: The fourth prototypical barrier in the diagram of Fig. 2a is NH_3 desorption from $2N\__3.NH_3.H$, and is estimated using the formula:

$$\text{Barrier (5)} = \Delta E\{2N\__3.NH_2.H + \tfrac{1}{2}H_2 \rightarrow 2N\__3.NH_3.H\} + \Delta H\{2N\__3.NH_2.H \rightarrow 2N\__3.H + NH_3\} + 0.355 \text{ eV} \quad (6)$$

4. Results and Discussion

The stability criterion narrows down the initial set of 34 candidate elements to: Ni, Co, and Cr. These were then tested for their ability to lower the four primary barriers in the reaction pathway. Table 1 lists the elements and how they reduce the barriers with respect to the pure Fe surface. The evolution of the barriers in Table 1 as a function of the dopant elements are visualized in Fig. 3. Cr was discarded by the third criterion of H_2 poisoning for increasing the reaction barrier. We predict that Ni will reduce the primary barrier by 0.1 eV further than Co so we choose Ni for further analysis over the reaction pathway. (Ni is also cheaper than Co).

Table 1. The energies for prototypical barriers are shown for Co, Cr, and Ni doping the Fe(111) catalyst subsurface, as well as for pure Fe(111). Barrier-overall reports the highest barrier among (1-4). The stability criterion is not shown in the table and the detailed values can be found in the supporting information. TOF estimated on a simplified kinetic model are also reported. Free energies in eV.

Element	Barrier-2	Barrier-3	Barrier-4	Barrier-5	Barrier-overall	Estimated TOF (S^{-1}, 673 K)
Ni	1.47	1.41	1.34	1.39	1.47	138
Co	1.57	1.53	1.44	1.41	1.57	24.5
Cr	1.68	1.69				
Fe	1.68	1.57	1.53	1.43	1.68	3.68

The addition of Ni to the sublayer of the Fe(111) structure reduces all four primary energy barriers in the reaction pathway. We can estimate the HB TOF under the given conditions via transition-state-theory as: $(k_BT/h)\exp[-\Delta G^{\dagger}_{overall}/k_BT]$, where $\Delta G^{\dagger}_{overall}$ is the largest (or overall) free-energy barrier, T is the temperature, k_B is the Boltzmann constant, and h is the Planck constant. This suggests that Ni subsurface doping will increase the turnover frequency to 138 NH_3/ s per site. Since Ni in the 2nd layer is more favorable than the top layer by 0.075 eV and more stable than the 3rd layer by 0.056 eV for the 4N state, we assume that Ni subsurface-doping is preferred over the entire reaction pathway. Fig. 4 illustrates the ammonia synthesis mechanism on the subsurface Ni-doped (2 x 2) unit cell of the Fe(111) surface to better illustrate the interaction of the molecules on the Fe(111) surface. The atomic coordinates of some key configurations ($3N\text{-}NH_2$/n, $2N\__3.NH_2.H\_c$, $2N\__3.2V\_b$ and $2N\__f.2H$) are given in SI.

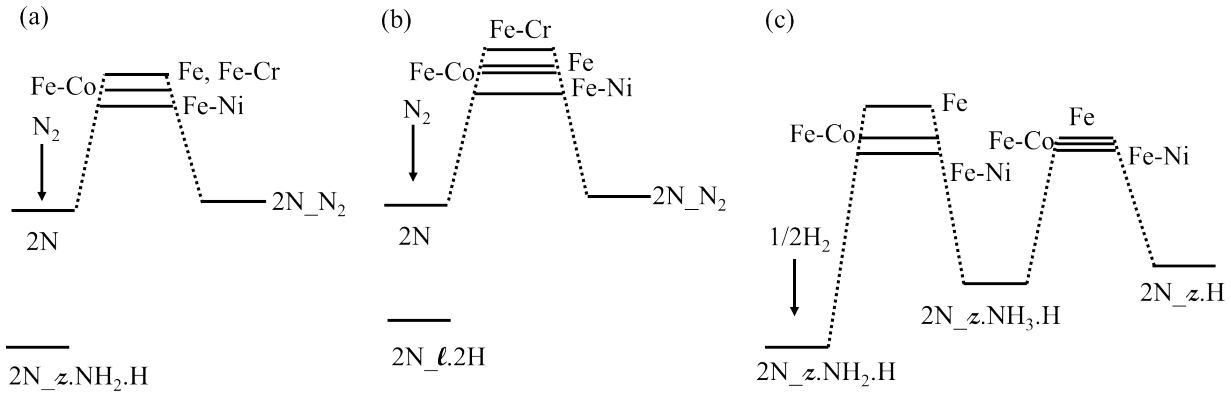

Figure 3. Evolution of the energy barriers used in the HHCTS protocol as a function of subsurface dopant element: (a) adsorption/dissociation of N_2; (b) H_2 poisoning (c) H migration and NH_3 desorption.

The primary reaction barrier reduced by the inclusion of Ni involves the difference between the adsorption saddle-point of N_2 onto the $2N\__j$ state with respect to the $2N\__j.NH_2.H$ dynamical resting state. The intermediate $2N\__j$ state is a zigzag configuration, with two empty sites or vacancies next to each other on the surface N_2 absorbs and dissociates on this state to occupy the empty sites, creating a configuration with N's in all available locations on the top layer, the 4N state. The primary barrier is reduced from 1.68 eV on the pure Fe(111) surface to 1.47 eV on the Ni-doped Fe(111) surface, which arises from the stabilization of the $2N\__j$ configuration while the adsorption barrier component remains the same on the two surfaces.

The second prototypical barrier is associated with the $2N\__{\ell}.2H$ linear configuration that can become the dynamical resting state and slow down the catalytic process. This consists of the free-energy difference between this configuration and the $2N\__j$ state, plus the N_2 adsorption barrier onto $2N\__j$. This second barrier is significantly reduced from 1.57 on the pure Fe surface to 1.38 on the doped Fe surface, again due to stabilization of the $2N\__j$ configuration.

The third prototypical barrier is the hydration of NH_2 to create NH_3 the Langmuir-Hinshelwood step: $2N\__j.NH_2.H$ into $2N\__j.NH_3$ (or better $2N\__j.NH_2.H$ into $2N\__j.NH_2.2H$ and then into $2N\__j.NH_3.H$). This third barrier is reduced from 1.52 eV on the pure Fe surface to 1.36 eV on the doped Fe surface.

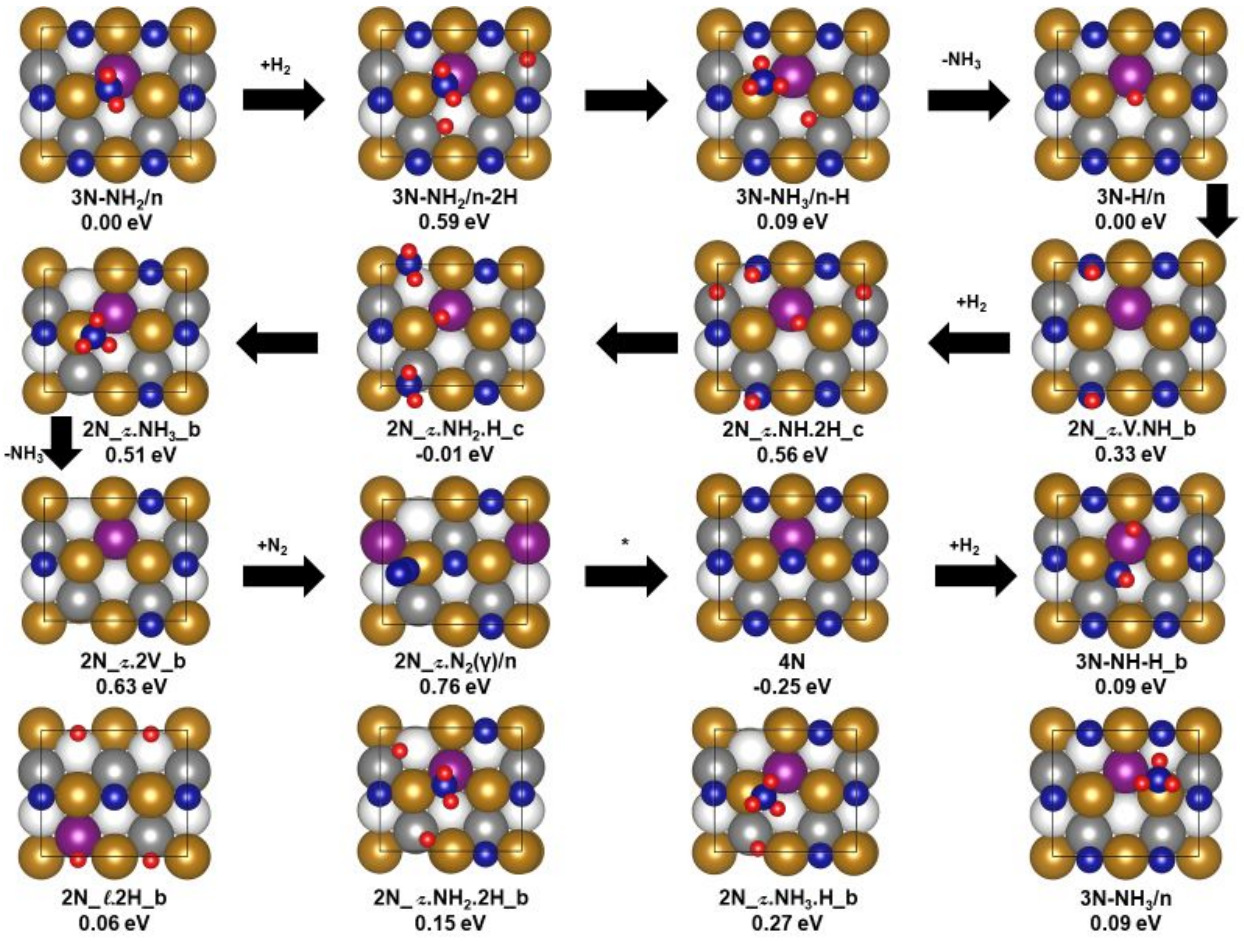

Figure 4. The step-by-step reaction process for NH_3 synthesis on sublayer Ni doped Fe(111) structure. The asterix (*) identifies the steps where the N_2 dissociates on the surface to form the 4N configuration. Four alternative structures are included for consideration in the pathway. Free energies at 673 K and pressures of H_2 = 15 atm, N_2 = 5 atm, and NH_3 = 1 atm is in eV. The letters a, b, and c represent which species of the molecular formula the doped element is closest to. For example, 2N_ℓ.2H_b, the b is denoting that the doped element is closest to the H, the second species mentioned in the molecular formula.

The fourth prototypical barrier is NH_3 desorption. The highest desorption energy would be associated with the 2N_ℓ.NH_3 state. This final barrier is reduced from 1.40 eV on the pure Fe surface to 1.28 eV on the doped Fe surface, because of decreased binding of N-species to the surface.

Since Fe is ferromagnetic, we analyzed magnetic moments (spins) and charges of the dopant atom and the nearby atoms to understand the role of the Ni in the energetics. We analyzed the 4N, 2N, 2N_ℓ.2H, and 2N_ℓ.NH_2.H states because they are involved in rate determining steps of the HB process. To understand the spin changes in Table 2, a qualitative valence bond (VB) model is employed. Here, we assume that each of the unpaired spins of N atom makes a covalent bond to an unpaired spin on the neighboring Fe atoms, reducing the spin by 3 units. Fig. 5 shows how Ni-subsurface doping affects the system magnetization, which we interpret in the Valence Bond scheme as due to spin pairing of the unpaired spin of the reactant with an unpaired spin on the Fe: the magnitude of the spin on the metal

atoms decreases by ~ 0.8 as a new bond is formed to the adsorbate N-species, or it increases as the bond is broken. Most significant is that Ni-doping has a major effect on the 2N state, dramatically decreasing the spin of subsurface Fe atoms near Ni by ~1.3, suggesting a much stronger N-Fe bond. In contrast, for the 4N state the spin of the Fe atoms increases upon Ni doping, while the spin of doped Ni atom decreases, leading to an overall increase of spin, which suggests that N is more weakly bound to the surface. This analysis is consistent with the energy diagrams of Figs. 2a and 5 showing that the 2N state is stabilized whereas the 4N state is destabilized for the Ni-doped system. Considering the other two important configurations: 2N_ℓ.2H, and 2N_ʒ.NH_2.H, we find that the spin of Fe atoms does not change significantly, which agrees with the QM energy diagram in which the energy of these two states is similar for pure Fe(111) and Ni-doped system. These results are consistent with previous research on how intermediates adsorbed on a metal surfaces make valence bonds to a metal surface.[26-29] We also report in Table 2 the total magnetic moment of the given configurations, showing a decrease in the total magnetic moment for the 2N, 2N_ℓ.2H, and 2N_ʒ.NH_2.H configurations and an increase for 4N configuration upon Ni doping. Table 2 also displays the change in the ΔG of the pure and doped structures, but this does not allow for a simple interpretation. We conclude that such a spin pairing analysis may play an important role in designing catalysts to accelerate the Haber-Bosch reaction, but further research is required to fully understand its detailed implications.

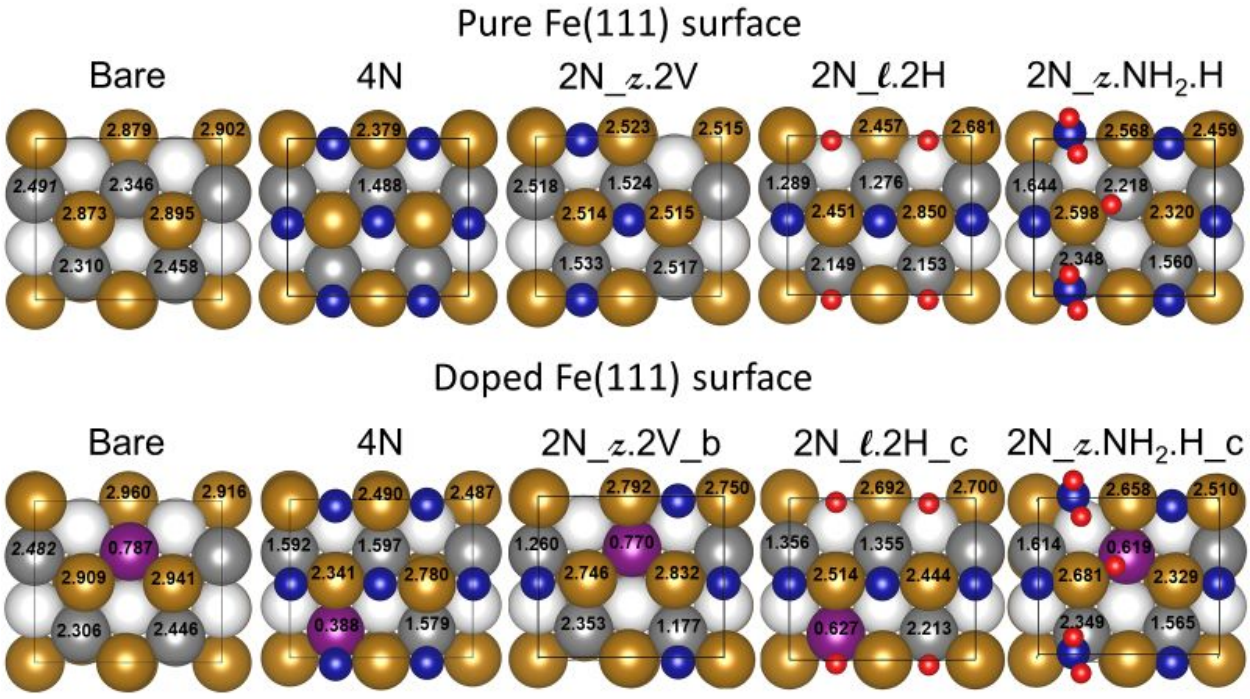

Figure 5. The magnetization of the Ni atom and the atoms around it are shown on the pure and doped Fe(111) surface to show how Ni effects the magnetization due to spin-spin bonding.

Table 2. Magnetic moment charges of the important configurations of the doped structures in comparison to the same structure on the pure Fe(111) surface. Changes in ΔG (δ(ΔG)) refer to the free energy difference of various adsorbates between doped and pure Fe(111) surface. The approach to obtain the ΔG can be found in methodology section.

Species	Total mag (μB)	Total mag (μB) on pure Fe(111) surface	ΔMag (doped Fe(111) top two surfaces vs. pure Fe(111)	δ(ΔG) Fe_3Ni(111) vs. Fe(111)
4N	54.19	53.44	0.76	+0.17
2N	57.18	58.27	-1.09	-0.17
2N-2H	55.69	57.08	-1.39	+0.02
2N-NH_2-H	56.58	57.67	-1.08	+0.04
Bare	61.75	62.93	-1.18	

Table 3. Percent of populations (i.e., residence times) = t_i(%) for the most relevant configurations in (2x2) unit cells of the Fe(111) surfaces under steady-state of ammonia synthesis as predicted by kMC simulations at 673 K and H_2, N_2, NH_3 pressures as indicated (in atm) using QM data. Populations of all other states are below 1%, making up for the missing percent to 100%.

	$p(H_2,N_2,NH_3)=(15,5,1)$ **– Fe(111)**			$p(H_2,N_2,NH_3)=(15,5,1)$ **– Fe4//Fe_3Ni(111)**	
configuration	t_i (%)	apparent ΔG	configuration	t_i (%)	apparent ΔG
3N.NH_2	23.1	0.00	3N.NH_2	30.2	0.00
3N.NH_3.H	0.1	0.30	3N.NH_3.H	5.0	0.10
3N.H	5.1	0.09	3N.H	23.7	0.01
2N_3.NH_2.H	52.6	-0.05	2N_3.NH_2.H	26.9	0.01
2N_3.NH_2.2H	6.9	0.07	2N_3.NH_2.2H	1.7	0.17
2N_f.2H	7.1	0.07	2N_f.2H	6.5	0.09
2N_3.2H	2.2	0.14	2N_3.2H	5.0	0.10
4N	2.8	0.12	4N	0.5	0.23
TOF from kMC NH_3 mol/s/(2x2)	4.5		TOF from kMC NH_3 mol/s/(2x2)	72.0	

5. QM Free-Energy diagram and kinetic simulations for the Ni-doped Fe(111) catalyst

Exploiting the HHTCS approach allowed us to decrease the candidates for subsurface doping from 34 to 2 (Ni and Co). Since Ni is the most promising dopant by ~0.1 eV, we conducted a full QM analysis only for the Ni doped Fe(111) catalyst. As in ref 16, we focused on a streamlined reaction path involving 21 configurations and 13 barriers that are important for the kinetics. We note here that the number of possible configurations for the HB process on the Ni-doped surface are more than double the number for the pure Fe case. In Fig. S3 of the SI, following the lines of ref 30 where we considered first-layer doping, we introduce a nomenclature that unambiguously singles out all possible configurations in a (2x2) bcc(111) unit cell at subsurface doping of 0.25 ML with up to 3 different species adsorbed in bridge sites, and use this nomenclature throughout the article.[30]

The QM simulations were carried out for a (2 × 2) unit cell of the Fe(111) surface which was doped in the second layer with a Ni atom. Of the possible configurations illustrated in Fig. S3 of the SI, we restricted to the ones leading to the lowest-energy path (lowest-energy branch). The corresponding reaction energy diagram is shown in Fig. 6. We then used these free energies to predict HB TOF under steady-state conditions via a kinetic Monte Carlo (kMC) approach[31]. We used the same protocol as in ref 16: kMC kinetic constants were evaluated using transition state theory (TST)[32] as $(k_BT/h)\exp(-\Delta G^{\dagger}/k_BT)$, with $\Delta G^{\dagger}$ the corresponding free-energy barrier. For reactions involving gas-phase species adsorbing on the surface, we used TST for the reverse desorption process, and the microscopic reversibility principle. Typically, we used 20 independent replicas and 2 x 10^{10} kMC steps in each replica, testing that the results so produced are converged within 5% in the production rate. This corresponds to ~ 76 minutes of real time.

We focused on conditions of $P(H_2)$ = 15 atm, $P(N_2)$ = 5 atm, $P(NH_3)$ = 1 atm, and T=673°K, which are realistic target operating conditions for a less energy-demanding HB process. To achieve an unbiased comparison, we contrasted pure Fe and Ni-doped systems using a corresponding set of states and identical numerical parameters. Representative results are reported in Table 3, where we include for the dominant configurations of the (2x2) unit cell the following quantities as predicted by the kMC: turn-over-frequency (TOF), per-cent populations (i.e., per-cent residence times), and apparent free energy differences [evaluated as minus the logarithm of ratio of populations = P_i/P_0, where the reference states are chosen as $P_0 = P_{3N\_NH2}$]. On pure Fe(111), we predict a TOF of 4.5 NH_3/s per (2 × 2) site, which can be compared to TOF = 3.68 from our simplified model. On Ni-subsurface-doped Fe(111), this leads to a predicted TOF = 72.0 NH_3/s per (2 × 2) site, which can be compared to 138 in our simplified model.

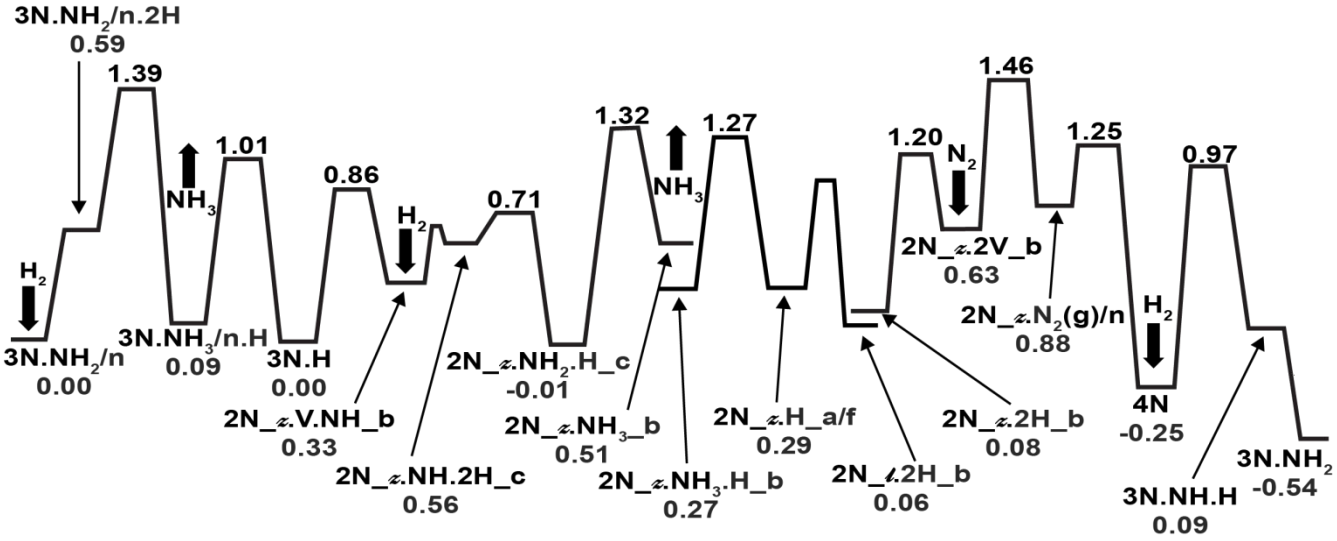

Figure 6. The standard free energy diagram (minimum energy path) for the Ni subsurface doped Fe(111) structure. Black shows the linear pathway, and green line shows the alternative pathway to minimize reaction barriers. Free energies are shown in eV.

The reason why Ni-subsurface doping accelerates the HB reaction rate has been clarified above, and is connected with the decrease in the largest primary barrier, associated with the free-energy difference between the adsorption saddle-point of N_2 onto the $2N\__i$ state with respect to the $2N\__i.NH_2.H$ dynamical resting state. In other words, Ni-doping stabilizes the $2N\__i$ configuration by 0.17 eV and destabilizes the $2N\__i$.NH2.H configuration by 0.04 eV, resulting in a decrease of the first primary barrier by 0.21 eV. The smaller increase in TOF from actual kMC simulations with respect to estimates based on the simplified (overall-barrier) model is caused by the fact that the Ni-doped Fe(111) surface approaches an ideal catalyst, in which all the minima in the free-energy diagram are iso-energetic and all primary barriers have similar values. However the multi-step path leads to a slower kinetics with respect to a one-step model. We can generalize the 1-barrier formula used in Table 1 (illustrated visually for greater clarity in Fig. S2a of the SI) to the 2-barrier case (illustrated in Fig. S2b of the SI) as follows: $1/k = 1/k_1 + 1/k_2 + \exp(\Delta G_2 - \Delta G_1)/(k_1 + k_2)$, where k is the overall reaction rate, k_1 and k_2 are the kinetic constants (rates) of the two individual mechanistic steps, while ΔG_1 and ΔG_2 are the corresponding free-energy barriers. Using this formula in the present case suggests a decrease in reaction rate by roughly by a factor of 2 with respect to the single-barrier model, in good agreement with the reduction in reaction rate observed from 138 $NH_3/s/(2 \times 2)$ in our simplified model to 72.0 $NH_3/s/(2 \times 2)$ in actual kMC simulations.

7. Conclusion

We used quantum mechanics (the Perdew-Burke-Ernzerhof (PBE-D3) flavor of Density Functional theory (DFT)) with hierarchical high-throughput catalyst screening (HHTCS)[16] to rationally design improved catalysts for the Haber-Bosch (HB) process. Starting with the free energy diagram of the HB process on bcc Fe(111), we defined four prototypical key mechanistic steps, whose barriers were arranged in decreasing order. Screening criteria were defined corresponding to the 4 prototypical barriers plus a second-layer stability test, and the candidate dopants in the subsurface layer at 0.25 ML doping were tested and narrowed down to the most promising.

Among the two final candidates for subsurface doping: Co and Ni, Ni showed the most promise (with barriers ~ 0.1 eV lower with respect to Co), and were selected for detailed analysis over the entire reaction pathway. This was followed by kMC simulations to determine the rates. The subsurface Ni-doped Fe(111) surface was predicted to increase the TOF of the Haber-Bosch process by a factor of 16 with respect to pure Fe(111), leading to a predicted TOF of 72 NH_3/s per (2 x 2) site. This was rationalized via Valence Bond analysis, showing that the increase in HB rate is due to stronger bonding to the surface of the 2N state compared to the 4N state.

These results indicated that the HHTCS computational approach is beneficial for testing quickly numerous candidate catalysts, narrowing the list down to a small set of most promising candidates quickly and efficiently. The use of an iron catalyst for the HB process is practical since it is cheap and there is a great deal of industrial experience on it. Subsurface doping of the Fe(111) catalyst is safer for the environment than Ru and far more earth-abundant. The predicted increase in TOF for Ni-doped Fe(111) could significantly reduce the cost of the Haber-Bosch process. Thus maintaining the same conditions and industrial plants used presently. Indeed, at 773 K and xx atm total pressure (25 atm H_2, 8.3 atm N_2 and 1 atm NH_3 pressure) we find a HB rate of 140 NH_3/s per (2 × 2) site on Ni-doped Fe(111), the same as the HB rate on pure Fe(111) at 773 K and 201 atm (150 atm H_2, 50 atm N_2 and 1 atm NH_3).[15] Thus, the total reactant pressure can be reduced by a factor of x and lead to the current production rate as HB on pure Fe. This prediction awaits experimental validation, e.g., by catalytic experiments on Fe single-crystal surfaces (or films) doped with controlled amount of deposited and alloyed Ni (e.g., followed via core-electron spectroscopies).

Further refinements of this research could include corrections to the DFT/PBE-D3 energetics,[16,33] changing the screening criteria to explore more possibilities, or considering other alterations of the catalyst,[34] such as multiple doping or the addition of promoters.

AUTHORS INFORMATION

Corresponding Authors

*E-mail: alessandro.fortunelli@cnr.it, wag@wag.caltech.edu, qia@unr.edu.

ORCID

Jon Fuller: 0000-0003-1233-7842

Alesandro Fortunelli: 0000-0001-5337-4450

William A. Goddard, III: 0000-0003-0097-5716

Qi An: 0000-0003-4838-6232

Acknowledgment This work was initiated by the U.S. Department of Energy (USDOE), Office of Energy Efficiency and Renewable Energy (EERE), Advanced Manufacturing Office Next Generation R&D Projects under contract no. DE-AC07-05ID14517 (program manager Dickson Ozokwelu, in collaboration with Idaho National Laboratories, Rebecca Fushimi). We would like to thank the Information Technology department at the University of Nevada, Reno for computing time on the High Performance Computing Cluster (Pronghorn). Some calculations were also carried out on the GPU-cluster at Caltech provided by DURIP (Cliff Bedford, program manager).

Supporting Information

The Supporting Information is available free of charge on the ACS Publications website at DOI:xxx. the DFT data of the HHCTS simulations; energy diagram showing the 4 prototypical schematic free-energy barriers used in HHTCS screening; visual depiction of the one-barrier and two-barrier kinetic models; all possible configurations with at most 3 absorbates on the surface (excluding 4N) from the reaction pathway of the subsurface doped Fe(111) (2 x 2) unit cell.

Notes

The authors declare no competing financial interest.

References

(1) Mittasch, A.; Frankenburg, W. Early Studies of Multicomponent Catalysts. In *Advances in Catalysis*; Frankenburg, W. G., Komarewsky, V. I., Rideal, E. K., Eds.; Academic Press, 1950; 2, 81–104.

(2) Aika, K.; Neilsen, A. *Ammonia: Catalysis and Manufacture*; Springer-Verlag: Berlin ; New York, 1995.

(3) Jennings, J. R. *Catalytic Ammonia Synthesis: Fundamentals and Practice*; Springer Science & Business Media, 2013.

(4) King, D. A., Woodruff, D. P. *The Chemical Physics of Solid Surfaces and Heterogeneous Catalysis*; Elsevier Scientific Pub. Co. : New York, 1981.

(5) Ertl, G., Knözinger, H., Weitkamp, J. *Handbook of Heterogeneous Catalysis*; VCH: Weinheim, 2008.

(6) Schlögl, R. Catalytic Synthesis of Ammonia—A "Never-Ending Story"? *Angew. Chem. Int. Ed.* **2003**, *42*, 2004–2008.

(7) Hara, M.; Kitano, M.; Hosono, H. Ru-Loaded C12A7:E $^-$ Electride as a Catalyst for Ammonia Synthesis. *ACS Catal.* **2017**, *7*, 2313–2324.

(8) Ma, Z.; Zhao, S.; Pei, X.; Xiong, X.; Hu, B. New Insights into the Support Morphology-Dependent Ammonia Synthesis Activity of Ru/CeO2 Catalysts. *Catal. Sci. Technol.* **2017**, *7*, 191–199.

(9) Ni, J.; Wang, R.; Kong, F.; Zhang, T.; Lin, J.; Lin, bingyu; Wei, K. Highly Efficient Ru-Ba/AC Catalyst Promoted by Magnesium for Ammonia Synthesis. *Chinese J. Catal.* **2011**, *32*, 436–439.

(10) Kugler, K.; Luhn, M.; Schramm, J. A.; Rahimi, K.; Wessling, M. Galvanic Deposition of Rh and Ru on Randomly Structured Ti Felts for the Electrochemical NH3 Synthesis. *Phys. Chem. Chem. Phys.* **2015**, *17*, 3768–3782.

(11) Yiokari, C. G.; Pitselis, G. E.; Polydoros, D. G.; Katsaounis, A. D.; Vayenas, C. G. High-Pressure Electrochemical Promotion of Ammonia Synthesis over an Industrial Iron Catalyst. *J. Phys. Chem. A* **2000**, *104*, 10600–10602.

(12) Zhou, F.; Azofra, L. M.; Ali, M.; Kar, M.; Simonov, A. N.; McDonnell-Worth, C.; Sun, C.; Zhang, X.; MacFarlane, D. R. Electro-Synthesis of Ammonia from Nitrogen at Ambient Temperature and Pressure in Ionic Liquids. *Energy Environ. Sci.* **2017**, *10*, 2516–2520.

(13) Ogura, K.; Takagi, M. The Photoelectrochemical Conversion of Nitric Oxide into Ammonia at P-Gallium Arsenide in the Presence of Transition Metal Ions and Their Complexes. *J. Electroanal. Chem. Interfacial Electrochem.* **1985**, *183*, 277–284.

(14) Furuya, N.; Yoshiba, H. Electroreduction of Nitrogen to Ammonia on Gas-Diffusion Electrodes Loaded with Inorganic Catalyst. *J. Electroanal. Chem. Interfacial Electrochem.***1990**, *291*, 269–272.

(15) Qian, J.; An, Q.; Fortunelli, A.; Nielsen, R. J.; Goddard III, W. A. Reaction Mechanism and Kinetics for Ammonia Synthesis on the Fe(111) Surface. *J. Am. Chem. Soc.* **2018**, *140*, 6288–6297.
(16) An, Q.; Shen, Y.; Fortunelli, A.; Goddard III, W. A. QM-Mechanism-Based Hierarchical High-Throughput in Silico Screening Catalyst Design for Ammonia Synthesis. *J. Am. Chem. Soc.* **2018**, *140*, 17702–17710.
(17) Perdew, J. P.; Burke, K.; Ernzerhof, M. Generalized Gradient Approximation Made Simple. *Phys. Rev. Lett.* **1996**, *77*, 3865–3868.
(18) Perdew, J. P.; Burke, K.; Ernzerhof, M. Generalized Gradient Approximation Made Simple. *Phys. Rev. Lett.* **1997**, *78*, 1396–1396.
(19) Johnson, E. R.; Becke, A. D. A Post-Hartree-Fock Model of Intermolecular Interactions: Inclusion of Higher-Order Corrections. *J. Chem. Phys.* **2006**, *124*, 174104.
(20) Grimme, S.; Antony, J.; Ehrlich, S.; Krieg, H. A Consistent and Accurate *Ab Initio* Parametrization of Density Functional Dispersion Correction (DFT-D) for the 94 Elements H-Pu. *J. Chem. Phys.* **2010**, *132*, 154104.
(21) Kresse, G.; Hafner, J. Ab Initio Molecular Dynamics for Liquid Metals. *Phys. Rev. B* **1993**, *47*, 558–561.
(22) Kresse, G.; Hafner, J. Ab Initio Molecular-Dynamics Simulation of the Liquid-Metal--Amorphous-Semiconductor Transition in Germanium. *Phys. Rev. B* **1994**, *49*, 14251–14269.
(23) Kresse, G.; Furthmüller, J. Efficiency of Ab-Initio Total Energy Calculations for Metals and Semiconductors Using a Plane-Wave Basis Set. *Comput. Mater. Sci.* **1996**, *6*, 15–50.
(24) Kresse, G.; Furthmüller, J. Efficient Iterative Schemes for Ab Initio Total-Energy Calculations Using a Plane-Wave Basis Set. *Phys. Rev. B* **1996**, *54*, 11169–11186.
(25) Dijkstra, E. W. A Note on Two Problems in Connexion with Graphs. *Numer. Math.* **1959**, *1*, 269−271.
(26) Kua, J.; Goddard III, W. A. Chemisorption of Organics on Platinum. 1. The Interstitial Electron Model. *J. Phys. Chem. B* **1998**, *102*, 9481–9491.
(27) Kua, J.; Goddard III, W. A. Chemisorption of Organics on Platinum. 2. Chemisorption of C2Hx and CHx on Pt(111). *J. Phys. Chem. B* **1998**, *102*, 9492–9500.
(28) Kua, J.; Faglioni, F.; Goddard III, W. A. Thermochemistry for Hydrocarbon Intermediates Chemisorbed on Metal Surfaces: CHn-m(CH3)m with n = 1, 2, 3 and m ≤ n on Pt, Ir, Os, Pd, Rh, and Ru. *J. Am. Chem. Soc.* **2000**, *122*, 2309–2321.
(29) Kua, J.; Goddard III, W. A. Oxidation of Methanol on 2nd and 3rd Row Group VIII Transition Metals (Pt, Ir, Os, Pd, Rh, and Ru): Application to Direct Methanol Fuel Cells. *J. Am. Chem. Soc.* **1999**, *121*, 10928–10941.
(30) Qian, J.; Fortunelli, A.; Goddard III, W. A. Effect of Co Doping on Mechanism and Kinetics of Ammonia Synthesis on Fe(1 1 1) Surface. *J. Catal.* **2019**, 370, 364-371.
(31) Gillespie, D. T. A General Method for Numerically Simulating the Stochastic Time Evolution of Coupled Chemical Reactions. *J. Comput. Phys.* **1976**, *22*, 403–434.
(32) Vineyard, G. H. Frequency Factors and Isotope Effects in Solid State Rate Processes. *J. Phys. Chem. Solids* **1957**, *3*, 121–127.
(33) Zaffran, J.; Michel, C.; Delbecq, F.; Sautet, P. Trade-Off between Accuracy and Universality in Linear Energy Relations for Alcohol Dehydrogenation on Transition Metals. *J. Phys. Chem. C* **2015**, *119*, 12988–12998.

(34) Foster, S. L.; Bakovic, S. I. P.; Duda, R. D.; Maheshwari, S.; Milton, R. D.; Minteer, S. D.; Janik, M. J.; Renner, J. N.; Greenlee, L. F. Catalysts for Nitrogen Reduction to Ammonia. *Nat. Catal.* **2018**, *1*, 490–500.

Table of Contents Graphic

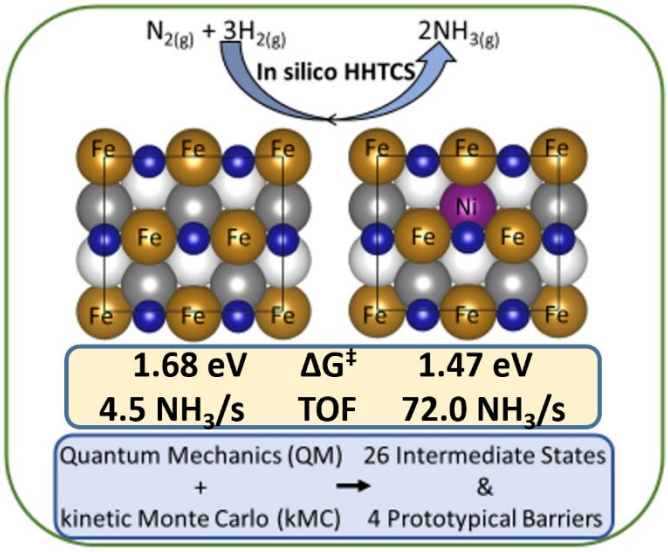

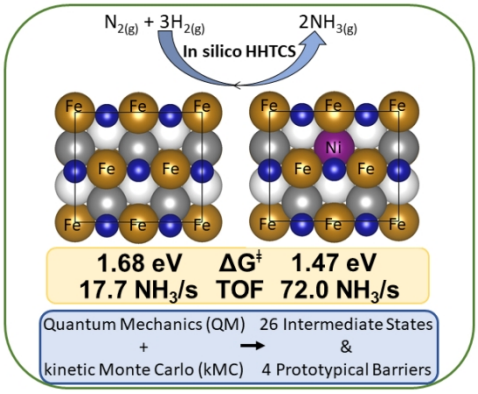

338x190mm (96 x 96 DPI)